

SUPPORTING INFORMATION

Externally-applied electric fields up to 1.6×10^5 V/m do not affect the homogenous nucleation of ice in supercooled water

Claudiu A. Stan, Sindy K. Y. Tang, Kyle J. M. Bishop, and George M. Whitesides*

Department of Chemistry and Chemical Biology, Harvard University,

Cambridge, MA 01238 USA

Abstract. This supporting information file contains: i) details of the construction of microfluidic devices made for the study of the nucleation of ice in external electric fields, ii) the derivation of equations 2, 3, and 4 in the manuscript, iii) a description of the electrical circuit used to supply and record the electric fields, iv) results from three measurements of nucleation in the presence of electric fields with frequencies of 3, 10 and 30 kHz, v) description and results of the numerical modeling of electric fields inside the microfluidic device, vi) a description of the procedure used to calculate the sensitivity of measurements of the rate of nucleation, and vii) the derivation of equation 12 in the manuscript.

* corresponding author, e-mail: gwhitesides@gmwgroup.harvard.edu

1. Fabrication of the microfluidic device.

The microfluidic devices used in our nucleation experiments in the presence of electric fields are similar to the ones that we used previously to measure the rates of nucleation of ice in supercooled water¹. The channel and nozzle are of the first design listed in table ST-1 in the supplementary information of Ref.1, which also describes the construction and assembly of the devices. The difference from the devices described in Ref. 1 consists of the use of high voltage electrodes instead of microfabricated thermometers.

Figure S1 shows the actual construction of the structure described in Figure 1b. The ground electrode is a 200-nm thick Pt layer sputtered on a 50×75×1 mm microscope slide made from soda-lime glass. Top electrodes were cut with a diamond saw from 1.1 mm-thick, ITO-coated float glass slides (Delta Technologies, Ltd.). Wires connected both electrodes to the rest of the electrical circuit. The wire for the bottom electrode was simply soldered with indium to the Pt layer, but the electrical connection of the top electrodes required special precautions to avoid the formation of regions of low dielectric strength between electrodes. Figure S1a shows the construction of top electrodes: we first polished their edges to a smooth shape, then we sputtered Pt over the edges to create an electrical via connection between the bottom and the top of the slide, and we soldered the wire to the top of the slide.

The dielectric spacers (see Figure 1b) were made from 150-micron thick glass coverslips (NeuroScience Associates), and glued to electrodes using epoxy resin (Duralco 4462, Cotronics Corp.). To reduce the thickness of the bonding layer of resin, we pressed the slide and the coverslip together using a vise; the final thickness of the bonding layer varied between 5 and 20 microns.

Figure S1b shows a picture of a microfluidic device for the study of nucleation under external electric fields. The devices had two identical independent channels, and each channel had its own high-voltage electrode; the grounding electrode was common to the whole device. A third electrode, placed over the inlet and nozzle area, was kept at the same potential as the ground electrode; the purpose of the third electrode was to screen near the nozzle the electric fields generated by the high voltage electrodes; these fields might affect the generation of drops.

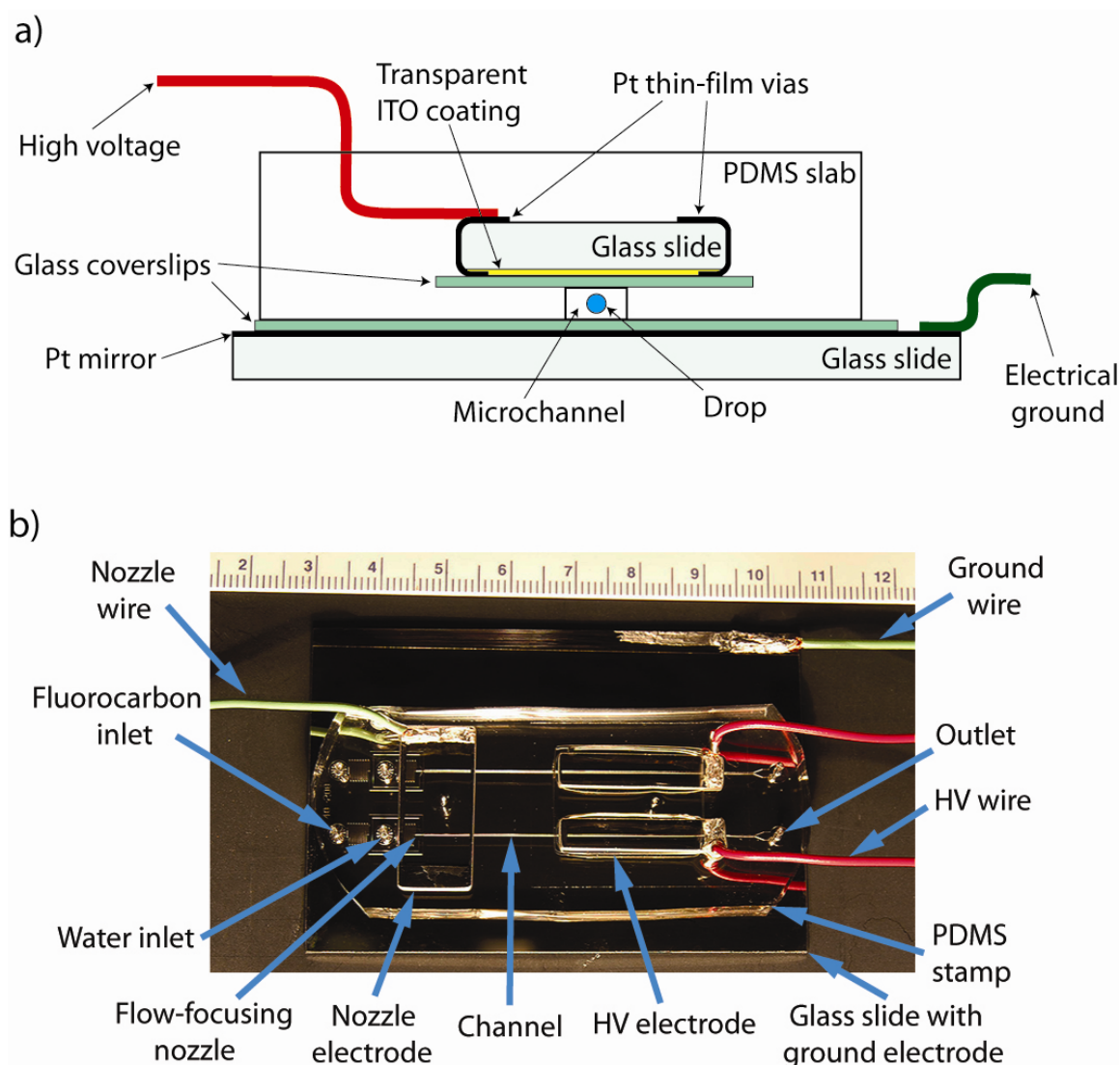


Figure S1. The construction of microfluidic devices for nucleation experiments in electric fields. a) Schematic of a cross-section through the device (not to scale) showing how the electrodes were assembled and connected. We embedded the top electrodes in a PDMS slab prior to curing; after curing we bonded the slab to the bottom electrode. b) Picture of one microfluidic device. The devices had two identical channels that could be used independently. High voltage electrodes apply a strong electric field on a section of the channel ~ 25 mm long, and a third grounded electrode placed over nozzles screened the drops from electric fields. The units on the ruler on top of the image are centimeters.

2. Derivation of equations 2 to 4.

2.1. Periodic variables and their rate of change. The mechanisms that lead to the screening of electric fields in water do not act instantaneously after the external electric field changes; instead, the electric field decays to a fraction f of its initial value in a characteristic time, τ_{equil} . We choose f to be approximately equal to $1/e$ (here e is the base of the natural logarithm) since many equilibration mechanisms lead to an exponential decay of deviations from the equilibrium values. We can define the rate of change characteristic to an equilibration mechanism, ω_{equil} , as the inverse of the equilibration time τ_{equil} . (Eq. S1).

$$\omega_{equil} = \frac{1}{\tau_{equil}} \quad \text{Eq. S1}$$

The *rate* of change of a periodically-varying variable is higher than the *frequency* of the change; during one period of oscillation, the variable evolves four times between its extreme values and the mean value. In the case of a sinusoidally-varying variable the relation between the *frequency* of the variable, $f_{periodic}$, and its *rate of change*, $\omega_{periodic}$, is given by Eq. S2:

$$\nu_{periodic} = \frac{\omega_{periodic}}{2\pi} \quad \text{Eq. S2}$$

For our screening problem, we can define a screening frequency, f_{screen} , which is related to the screening rate ω_{screen} by Eq. S3.

$$f_{screen} = \frac{\omega_{screen}}{2\pi} \quad \text{Eq. S3}$$

To create fields inside water, the frequency of an external AC field, f_{AC} , must be larger than f_{screen} ; combining this condition with Equation S3 we arrive at Equation 4.

2.2. Autoionization. Natzle and Moore² determined experimentally the time in which an excess concentration of H^+ and OH^- in pure liquid water decays to $1/e$ of its initial value. At room temperature (300 °K) this decay time, τ_{auto} , is equal to approximately 50 microseconds. We can calculate using Equation S1 the rate of screening due to autoionization at room temperature, ω_{auto} ; the result is Equation 2.

2.3. Electrical screening by diffusing electrical charges. Screening of electric fields by a material involves a redistribution of free charges present in the material until the

field generated by these charges creates a screening field that cancels the external field. To estimate the rate of screening in water, we use a system that is composed of a flat interface between water and air; an external field that is perpendicular to the interface and has a magnitude $E_{external}$ is applied instantaneously on the system. The electric field inside water, E_{water} , is initially equal to the field in air, but it is rapidly reduced by a factor equal to the dielectric constant of water, ϵ_w , as water molecules polarize and reorient their dipole moments in response to the field. This reduction in the field is completed in a time on the order of a nanosecond, which is much faster than the rate at which our external fields vary; therefore the field in water is given by Eq. S4:

$$E_{water} = \frac{E_{external}}{\epsilon_w} \quad \text{Eq. S4}$$

Eventually, magnitude of the electric field in water drops to zero as free H^+ and OH^- ions drift due to the field E_{water} and build up surface charge at the air/water interface. This surface charge creates an electric field, E_{Debye} , which opposes E_{water} and grows until it cancels it.

The surface charge is distributed in a thin layer near the surface: the Debye layer. We can use Equation S5 to estimate the timescale of formation the Debye layer, τ_{Debye} , as the time in which an ion with a mobility μ_i drifts under the effect of the electric field of intensity E_{water} over the thickness of the Debye layer δ_{Debye} :

$$\tau_{Debye} = \frac{\delta_{Debye}}{\mu_i E_{water}} \quad \text{Eq. S5}$$

The electrical field produced in water by the charge in the Debye layer, E_{Debye} , is given by Eq. S6, where ϵ_0 is the permittivity of vacuum and σ_{Debye} is the surface density of charge in the Debye layer.

$$E_{Debye} = \frac{\sigma_{Debye}}{\epsilon_0 \epsilon_w} \quad \text{Eq. S6}$$

We estimated σ_{Debye} assuming that either only positive or only negative ions are present in the Debye layer, and that the spatial density of ions is equal to the equilibrium density of ions in water, n_0 (Eq. S7):

$$\sigma_{Debye} = e n_0 \delta_{Debye} \quad \text{Eq. S7}$$

In Eq. S7, e_e is the charge of the electron. Combining Eq. S5 to S7, we deduce a formula for τ_{Debye} (Eq. S8):

$$\tau_{Debye} = \frac{\epsilon_0 \epsilon_w}{e_e n_0 \mu_i} \quad \text{Eq. S8}$$

Equation 3 follows from Eq. S8 if we define the rate of screening due to charge diffusion, ω_{Debye} , to be the inverse of the timescale of formation the Debye layer τ_{Debye} .

3. The electrical circuit.

The electrical circuit (Figure S2) supplied alternating high-voltage potentials across the microfluidic device, and monitored and recorded these voltages during experiments. The high voltages were measured at the output port of the amplifier rather than at the device; we supplied small voltages from the signal generator ($\sim 1V$ peak-to-peak amplitude) to confirm that the amplitudes of voltages at the source and at the device were equal.

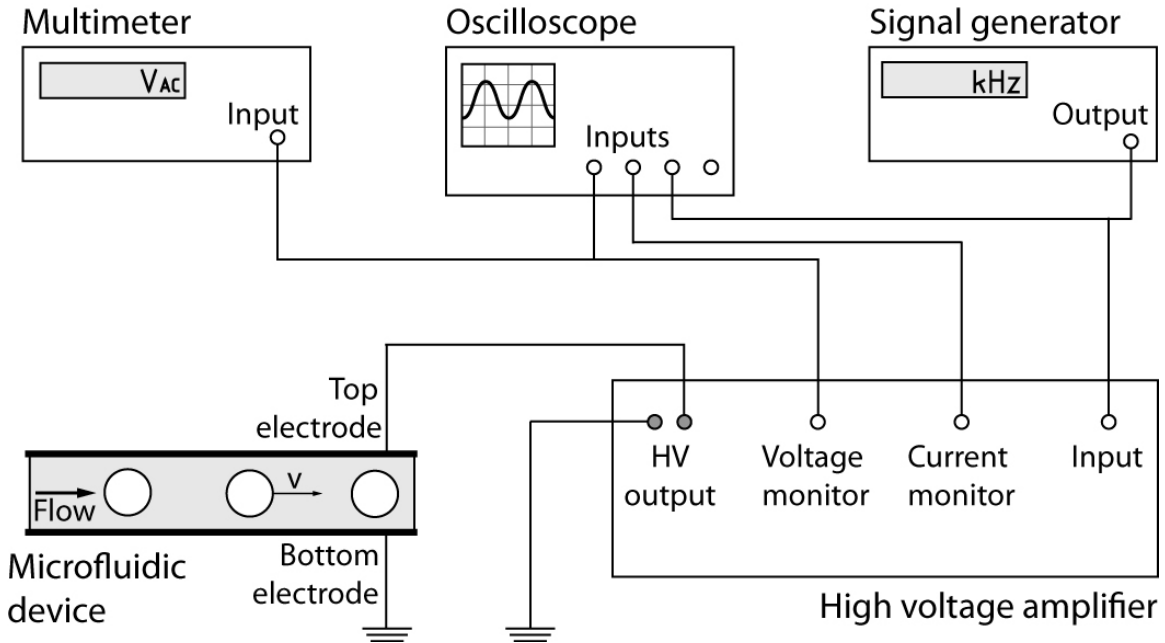


Figure S2. Schematic of the electrical circuit used in experiments. The high voltage amplifier provided both high voltages for experiments, and scaled-down voltages for recording and monitoring. The oscilloscope recorded the shape of the alternating voltage, while the multimeter recorded the effective value of the voltage during the whole duration (tens of minutes) of an experiment.

4. Measurements at other frequencies of the electric field.

Figure S3 shows the results of freezing experiments for electric field frequencies of 3, 10, and 30 kHz. The voltage at which premature freezing occurs increases with frequency. Lower frequencies induce larger oscillations of the shape of the drop; the drop thus starts to sample regions with colder carrier fluid at smaller applied voltages.

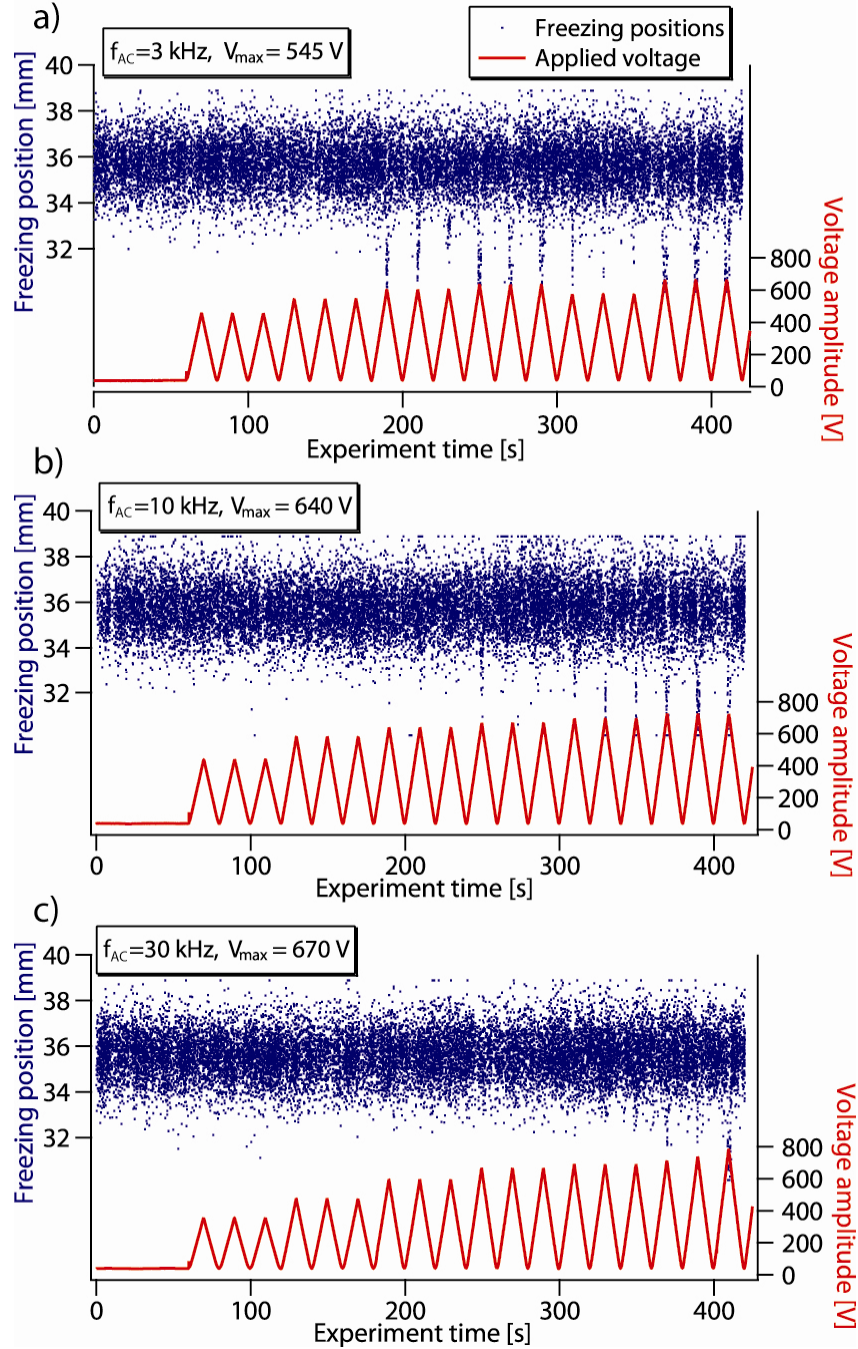


Figure S3. Freezing experiments in the presence of electric fields with frequencies of 3 kHz (19 358 drops), 10 kHz (19 341 drops), and 30 kHz (19 513 drops).

5. Numerical modeling of electric fields inside the microfluidic device.

5.1. Geometry and boundary conditions. Figure S4 shows the geometry of the numerical model and the notations that we used. The electric field inside the microfluidic device was calculated numerically using a commercially available finite element analysis package (COMSOL). The geometry used in the calculations is illustrated schematically above. A droplet of diameter D is positioned at the origin inside a rectangular channel of length L , width w , and height δ_3 ; the other dimensions are illustrated Figure S3. The electrostatic potential, ϕ , within each region i is governed by Laplace's equation (Eq. S9); we have neglected the effects of free charge (e.g., due to dissolved ions) as discussed in the manuscript.

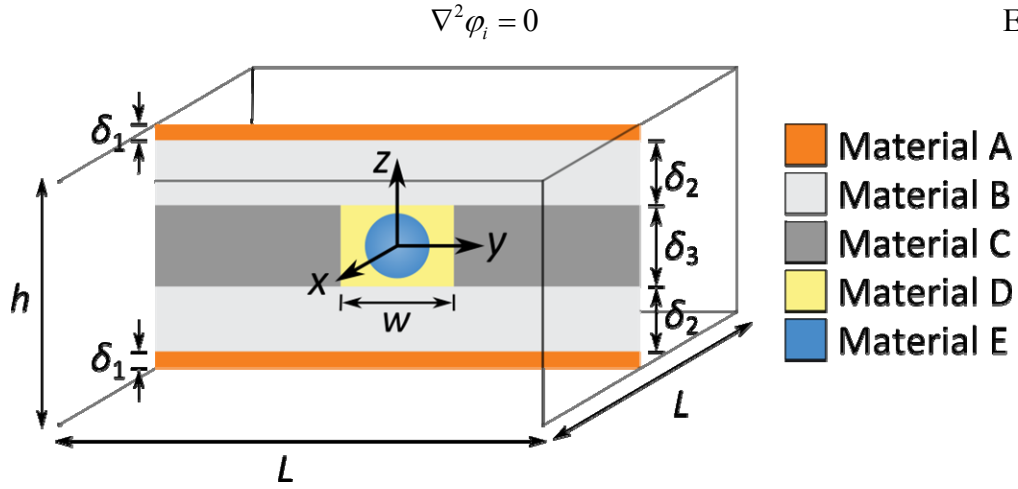


Figure S4. The geometry of the numerical model.

At the interfaces between the dielectric regions, the potential satisfies the following conditions (Eqs. S10–S14):

Internal Interfaces:

$$\phi_i = \phi_j \quad \text{Eq. S10}$$

$$(\epsilon_i \nabla \phi_i - \epsilon_j \nabla \phi_j) \cdot \mathbf{n} = 0 \quad \text{Eq. S11}$$

where ϵ_i is the dielectric constant of region i , and \mathbf{n} is the unit normal vector directed from region i to region j . Additionally, the top electrode ($z = h/2$) is maintained at a constant voltage V_0 ; the bottom electrode ($z = -h/2$) is grounded. At the other external boundaries, it is assumed that the field is directed only in the z -direction.

External Boundaries:

$$\varphi(z = h / 2) = V_0 \quad \text{Eq. S12}$$

$$\varphi(z = -h / 2) = 0 \quad \text{Eq. S13}$$

$$(\nabla \varphi) \cdot \mathbf{n} = 0 \text{ at } y = \pm L / 2 \text{ and } x = \pm L / 2 \quad \text{Eq. S14}$$

After solving for the electric potential throughout the domain, we compute the average electric field within the droplet, \mathbf{E}_{drop} , as (Eq. S15):

$$\mathbf{E}_{\text{drop}} = \int_{V_{\text{drop}}} -\nabla \varphi dV \quad \text{Eq. S15}$$

Because the field is not perfectly uniform within the drop, we also computed the variance $\sigma_{\text{drop},i}$ of each component i of the field about the mean value using Eq. S16:

$$\sigma_{\text{drop},i}^2 = \int_{V_{\text{drop}}} \left(-\frac{\partial \varphi}{\partial x_i} - E_{\text{drop},i} \right)^2 dV \quad \text{Eq. S16}$$

5.2. Numerical results. In this section of the supporting information, we expressed all electric fields as a fraction of the ‘average’ applied field, $E_0 = V_0 / h$. We calculated the magnitude of the field inside the drops for three cases: (1) using the most probable values of the experimental parameters; (2) using the limit values of experimental parameters that correspond to an upper limit of field; and (3) using the limit values of experimental parameters that correspond to a lower limit of the field. Case 1 corresponds to the most probable value of the field. Table ST-1 lists the experimental parameters of case 1 and the corresponding values of the electric field, and Figure S5 shows the magnitude of electric fields inside the device.

Table ST-1. Case 1: most probable parameter values, and corresponding electric fields.

Parameters			
δ_1	20 μm	ϵ_A (Epoxy)	4
δ_2	150 μm	ϵ_B (Glass)	6.7
δ_3	125 μm	ϵ_C (PDMS)	2.65
w	200 μm	ϵ_D (PFMD)	2.13
D	70 μm	ϵ_E (water)	110

Results			
	$i = x$	$i = y$	$i = z$
$E_{\text{drop},i} / E_0$	0	0	0.110
σ_i / E_0	4.0×10^{-4}	3.3×10^{-4}	6.1×10^{-4}

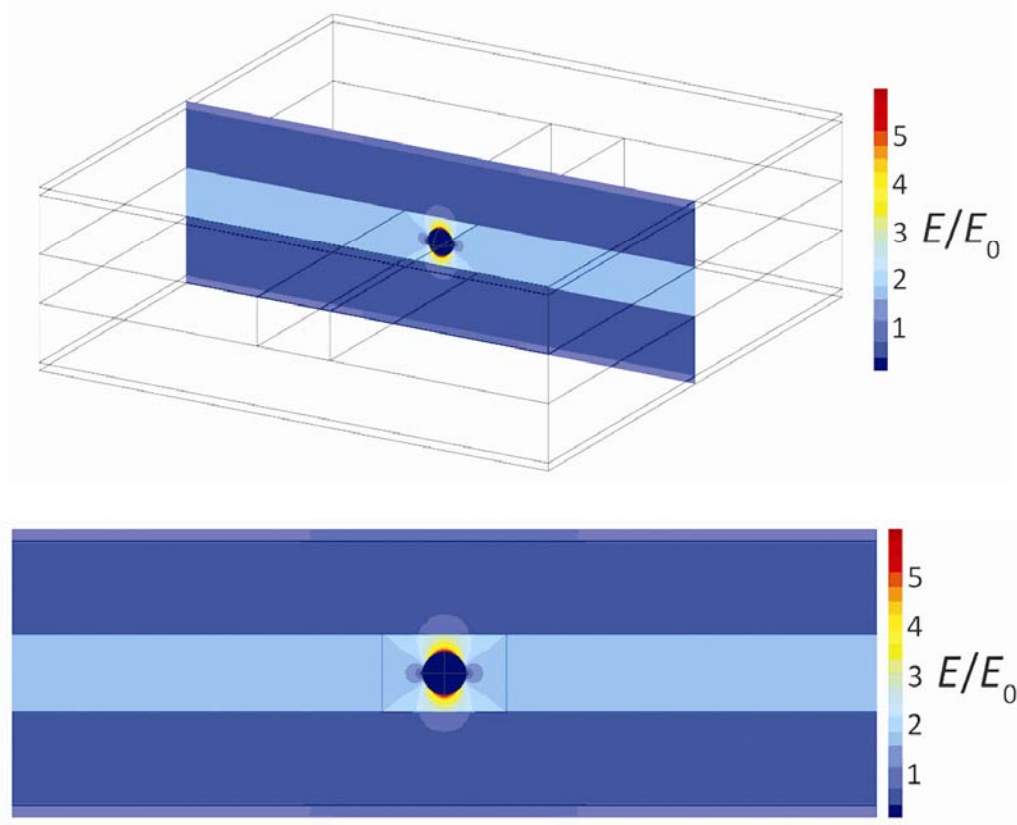


Figure S5. The magnitude of the electric field, E , scaled by the applied field $E_0 = V_0/h$. This field was calculated using the most probable values of experimental parameters (Case 1).

5.3. Estimation of the uncertainty in magnitude of the field. For small deviations about the most probable parameter values, the resulting electric field depends linearly on small changes in the values of parameters. The change in the magnitude of the electric field E is given by Eq. S18, and Table ST-2 lists experimental values of the slopes of variation of E with our experimental values; here we indicated the most probable values with an asterisk.

$$E_{drop,z} = E_{drop,z}^* + \left(\frac{\partial E_{drop,z}}{\partial \epsilon_A} \right)^* (\epsilon_A - \epsilon_A^*) + \left(\frac{\partial E_{drop,z}}{\partial \epsilon_B} \right)^* (\epsilon_B - \epsilon_B^*) + \dots \quad \text{Eq. S18}$$

Table ST-2. Linear coefficients of variation of the electric field with the parameters of the microfluidic device.

Parameters			
$(\partial E_{drop,z} / \partial \delta_1)^*$	$-5.2 \times 10^{-4} \mu\text{m}^{-1}$	$(\partial E_{drop,z} / \partial \varepsilon_A)^*$	2.4×10^{-3}
$(\partial E_{drop,z} / \partial \delta_2)^*$	$-3.0 \times 10^{-4} \mu\text{m}^{-1}$	$(\partial E_{drop,z} / \partial \varepsilon_B)^*$	6.7×10^{-3}
$(\partial E_{drop,z} / \partial \delta_3)^*$	$-5.4 \times 10^{-4} \mu\text{m}^{-1}$	$(\partial E_{drop,z} / \partial \varepsilon_C)^*$	-5.9×10^{-3}
$(\partial E_{drop,z} / \partial w)^*$	$1.9 \times 10^{-5} \mu\text{m}^{-1}$	$(\partial E_{drop,z} / \partial \varepsilon_D)^*$	2.8×10^{-2}
$(\partial E_{drop,z} / \partial D)^*$	$2.7 \times 10^{-4} \mu\text{m}^{-1}$	$(\partial E_{drop,z} / \partial \varepsilon_E)^*$	-9.7×10^{-4}

The linear coefficients in Table ST-2 indicate whether an increase in a given parameter will increase or decrease the value of the electric field. We used these correlations to select sets of upper and lower limits of experimental parameters that correspond to maximum (Case 2) or minimum (Case 3) values of the electric field. Table ST-3 lists the parameters and the fields of Case 2, and table ST-4 lists the parameters and the fields of Case 3.

Table ST-3. Upper limit of the magnitude of the electric field

Parameters			
δ_1 (low)	0 μm	ε_A (high)	4
δ_2 (low)	150 μm	ε_B (high)	7.75
δ_3 (low)	125 μm	ε_C (low)	2.65
w (high)	200 μm	ε_D (high)	2.13
D (high)	70 μm	ε_E (low)	100

Results			
	$i = x$	$i = y$	$i = z$
$E_{drop,i} / E_0$	0	0	0.142
σ_i / E_0	5.5×10^{-4}	4.5×10^{-4}	8.3×10^{-4}

Table ST-4. Lower limit of the magnitude of the electric field.

Parameters			
δ_1 (high)	30 μm	ϵ_A (low)	4
δ_2 (high)	150 μm	ϵ_B (low)	4.6
δ_3 (high)	140 μm	ϵ_C (high)	2.65
w (low)	200 μm	ϵ_D (low)	2.00
D (low)	70 μm	ϵ_E (high)	110

Results			
	$i = x$	$i = y$	$i = z$
$E_{drop,i} / E_0$	0	0	0.0800
σ_i / E_0	2.1×10^{-4}	1.3×10^{-4}	2.7×10^{-4}

For a voltage of 700 V applied on a device with a thickness of 465 microns, the field inside drop is 1.6×10^5 V/m, and the maximum and minimum values of the field are 2.0×10^5 V/m and 1.2×10^5 V/m; the magnitude of the field, including experimental uncertainties, is $1.6 \pm 0.4 \times 10^5$ V/m.

6. Calculation of sensitivity to changes in the rate of nucleation.

The goal of this calculation is expressing the minimum factor, K_{sens} , by which we can observe changes in the nucleation rate J_N relative to J_N^0 ; J_N the rate of nucleation in the presence of an external factor and J_N^0 the value of the nucleation rate in the absence of that factor. K_{sens} is thus defined by Eq. S19, and the calculation of sensitivity will express it as a function of the experimental parameters measured, *i.e.* the freezing positions of drops x_i (Eq. S20)

$$K_{Sens} = \frac{J_N}{J_N^0} \quad \text{Eq. S19}$$

$$K_{Sens} = f(x_i) \quad \text{Eq. S20}$$

Over the range of nucleation temperatures (-36 to -38 °C) the nucleation rate J_N^0 observed in our system¹ can be approximated by Eq. S21, where A and B are fitting constants and T is the absolute temperature in degrees Kelvin.

$$\log J_N^0(T) = A - BT \quad \text{Eq. S21}$$

Next, we express J_N by Eqs. S22 to S25:

$$\log J_N(T) = \log K_{sens} + A - BT \quad \text{Eq. S22}$$

$$\log J_N(T) = A - BT + B \frac{\log K_{sens}}{B} \quad \text{Eq. S23}$$

$$\log J_N(T) = A - B(t - \delta T) = \log J_N^0(T - \delta T) \quad \text{Eq. S24}$$

Equation S24 shows that within the range of temperatures in which drops nucleate ice homogenously, an increase in the nucleation rate by a factor K_{sens} is equivalent to a shift in the temperatures of nucleation, δT , that is given by Eq. S25:

$$\delta T = \frac{\log K_{sens}}{B} \quad \text{Eq. S25}$$

For the nucleation experiments reported here the relation between freezing temperatures and freezing positions was approximately linear, therefore we expressed the shift in the temperatures of nucleation, δT , as a function of the minimum observable shift in freezing positions, δx , the spread of freezing positions, Δx , and the spread of nucleation temperatures ΔT (Eq. S16):

$$\delta T = \frac{\delta x}{\Delta x} \Delta T \quad \text{Eq. S26}$$

Combining Eq. S25 with Eq. S26, we can then express K_{sens} as (Eq. S27):

$$K_{sens} = 10^{B \frac{\delta x}{\Delta x} \Delta T} \quad \text{Eq. S27}$$

Fitting the rate of homogenous nucleation from Ref. S1 with Eq. S21 we determined $B \cong 2^\circ \text{C}^{-1}$, and we used the spread of temperatures of nucleation from data in Ref. S1 to get $\Delta T \cong 2^\circ \text{C}$. The data shown in Figure 2 has a spread of freezing positions of $\Delta x \cong 7 \text{mm}$. To determine δx , we performed first a 100-point running average of the raw data to determine the approximate average of the freezing positions. We chose the number of points in the running average such that the intensity of the electric field is approximately constant during the time required for recording the number of data used in the running average. Recording 100 points requires 2 seconds of operation – equal to one tenth of the period of modulation of the electric field. δx was equal to three times the standard deviation of the running average during one cycle of the modulation of the

electric field; $\delta x \cong 0.3\text{mm}$. Using these values of B , δx , Δx , and ΔT , Eq. S26 gives $\delta T \cong 0.09^\circ\text{C}$, and Eq. 27 gives $K_{sens} \cong 1.5$.

7. Derivation of Equation 12.

7.1. Model. We will derive Equation 12 using a system of $N_w=1000$ molecules of water; this number is approximately equal to the number of molecules in a critical nucleus of ice during homogeneous nucleation. In our calculations we assumed that the surface energy between ice XI and supercooled water is the same as the one between ice Ih and supercooled water. Using this assumption, the difference in free energies is equal to the difference between the free energies of the bulk of the system.

7.2 The free energy of ferroelectric ice at 235 °K. The free energy of ice XI is equal to free energy of ice Ih at the temperature of the ferroelectric ordering transition, T_{XI-Ih} . We used this equality to estimate the difference between free energies of ices above T_{XI-Ih} . At T_{XI-Ih} the relation between thermodynamic functions is given by Eq. S28,

$$\Delta G_{XI-Ih}(T_{XI-Ih}) = \Delta H_{XI-Ih}(T_{XI-Ih}) - T_{XI-Ih} \Delta S_{XI-Ih}(T_{XI-Ih}) = 0 \quad \text{Eq. S28}$$

where $\Delta G_{XI-Ih}(T)$ is the difference between the free energies of the ferroelectric and hexagonal ice nuclei, and ΔH_{XI-Ih} and ΔS_{XI-Ih} are the differences between enthalpies, and between entropies, of the two nuclei. To evaluate $\Delta G_{XI-Ih}(T)$, we made the assumption that ΔH_{XI-Ih} and ΔS_{XI-Ih} do not depend on temperature. This assumption that ΔH_{XI-Ih} does not depend on temperature is supported by experimental measurements of the specific heat of ice XI; the difference between the specific heats of ice Ih and ice XI is negligible below T_{XI-Ih} ³. Above T_{XI-Ih} , ΔH_{XI-Ih} is likely to remain constant because it arises from electrostatic interactions between molecules⁴; electrostatic interactions in an ice crystal do not change significantly when the temperature is changed. The value of $\Delta G_{XI-Ih}(T)$ above T_{XI-Ih} is given by Eq. S29, in which we used Eq. S28 to express ΔH_{XI-Ih} as a function of ΔS_{XI-Ih} .

$$\Delta G_{XI-Ih}(T) = \Delta H_{XI-Ih} - T \Delta S_{XI-Ih} = -\Delta S_{XI-Ih}(T - T_{XI-Ih}) \quad \text{Eq. S29}$$

The difference in entropy between the two phases is caused by proton disorder in hexagonal ice. In hexagonal ice the configurational contribution to entropy per molecule, s , was calculated theoretically by Pauling⁵ to be $s = k_B \ln(3/2)$, where k_B is Boltzmann's

constant. Equation S30 gives the free energy of ferroelectric ice relative to the free energy of hexagonal ice:

$$\Delta G_{XI-Ih}(T) = N_w k_B (T - T_{XI-Ih}) \ln\left(\frac{3}{2}\right) \quad \text{Eq. S30}$$

7.3. Electrostatic contributions to free energy. A particle with a permanent electric dipole of moment p that has an absolute temperature T and is placed in an uniform external field of magnitude E will be influenced by the field such that on average, the projection of the dipole moment along the direction of the field is $\overline{p_E}$. The electrostatic free energy of the particle is equal to the electrostatic energy of the particle when the system is in thermodynamic equilibrium at temperature T . The free energy is thus given by Eq S31:

$$G_{E,particle} = -E \overline{p_E} \quad \text{Eq. S31}$$

The average of the dipole moment, $\overline{p_E}$, can be much smaller than p in weak electric fields because of thermal agitation. We can evaluate the magnitude of a strong electric field that orients dipoles against thermal agitation, E_p , using Eq. S32:

$$E_p \approx \frac{k_b T}{p} \quad \text{Eq. S32}$$

For a molecule of water in ice Ih ($p = p_w = 6.2 \times 10^{-30}$ C·m) at a temperature that is typical for homogenous nucleation ($T = 235$ °K), $E_{p,water} \approx 5 \times 10^8$ V/m; for a ferroelectric nucleus ($p \sim N_w p_w = 6.2 \times 10^{-27}$ C·m), $E_{p,nucleus} \approx 5 \times 10^5$ V/m. Since the largest fields that we might investigate experimentally in micron-sized samples of water have magnitudes between $E_{p,water}$ and $E_{p,nucleus}$, we made the simplifying assumptions that (i) the water molecules in the nucleus of ice Ih are not aligned along the field, and (ii) the ferroelectric nucleus, along with all molecules in it, is perfectly aligned with the field. The average dipole moments, $\overline{p_{E,Ih}}$ and $\overline{p_{E,XI}}$, of the hexagonal and ferroelectric nuclei are then given by Eqs. S33 and S34:

$$\overline{p_{E,Ih}} = 0 \quad \text{Eq. S33}$$

$$\overline{p_{E,XI}} = N_w p_w \quad \text{Eq. S34}$$

Equation S35 expresses the difference between the electrostatic free energies of the two nuclei, $\Delta G_{E,XI-Ih}$:

$$\Delta G_{E,XI-Ih} = -E(\overline{p_{E,XI}} - \overline{p_{E,Ih}}) = -EN_w p_w \quad \text{Eq. S35}$$

Adding the electrostatic contribution to the temperature-dependent formula for the difference of free energies (Eq.S30) we obtain the following formula for the total difference in free energies (Eq. S36):

$$\Delta G_{XI-Ih}(E, T) = N_w k_B (T - T_{XI-Ih}) \ln\left(\frac{3}{2}\right) - EN_w p_w \quad \text{Eq. S36}$$

Equation 12 was derived from Eq. S36 using the condition $\Delta G_{XI-Ih}(E_{ferro}, T_{nucl}) = 0$.

References

- (1) Stan, C. A.; Schneider, G. F.; Shevkoplyas, S. S.; Hashimoto, M.; Ibanescu, M.; Wiley, B. J.; Whitesides, G. M. *Lab Chip* **2009**, 9, 2293–2305.
- (2) Natzle, W. C.; Moore, C. B. *J. Phys. Chem.* **1985**, 89, 2605–2612.
- (3) Tajima, Y.; Matsuo, T.; Suga, H. *J. Phys. Chem. Solids* **1984**, 45, 1135–1144.
- (4) Buch, V.; Sandler, P.; Sadlej, J. *J. Phys. Chem. B* **1998**, 102, 8641–8653.
- (5) Pauling, L. *J. Am. Chem. Soc.* **1935**, 57, 2680–2684.